ADVANCED MATERIALS TECHNOLOGIES
www.advmattechnol.de

A Flexible Sensitive Visible-NIR Organic Photodetector with High Durability

Kai Pu, Zhuhua Xu, Yu Gao, Cong Zhao, Faheem Ershad, Yuan Li, Richard Wang, Cunjiang Yu, and Guodan Wei**

Low-cost, deformable visible-near-infrared (visible-NIR) photodetectors can be configured into non-planar shapes to meet emerging optical needs. However, it remains challenging to develop low-cost flexible visible-NIR photosensor with excellent mechanical deformability and high optical detectivity. Herein, we report a flexible visible-NIR organic photodetector (OPD) based on a blend film of D18:BTP-4F as the active layer on a polyethylene naphthalate substrate. Owing to the low exciton binding energy of BTP-4F and the preferred orientation of the D18:BTP-4F film, the as-fabricated OPD exhibits excellent self-powered optoelectronic performances with a high responsivity, high detectivity, and fast response time of 206 mA W^{-1}, 6.45 × 10^{12} Jones (1 Jones = 1 cm $Hz^{1/2}$ W^{-1}), and 9 µs at the wavelength of 800 nm and bias voltage of 0 V, respectively. After 1000 bending/releasing cycles with an angle of 150° at a radius of curvature of 3 mm, the current-voltage curves remain stable both measured under dark and light illumination, indicating obvious device operation robustness. The reliable linear photosensitivity of the as-obtained OPD is demonstrated by the photoresponse under a range of different incident light intensities and its practical application for wearable health monitoring such as heart rate measurement is well demonstrated. Furthermore, a flexible visible-NIR image sensor for imaging acquisition is shown by demonstrating 5 × 5 OPD array under 850 nm light irradiation. The collective results on blend film design, flexible device fabrication and characterization, and imager development shed light on sought-after visible-NIR photosensing and imaging systems.

1. Introduction

Low-cost, flexible visible-near-infrared (visible-NIR) photodetectors that are deformable and could be configured into complex three-dimensional non-planar shapes to meet emerging optical imaging needs, holds great many promising applications in artificial intelligence,[1,2] optical communication,[3,4] night vision,[5,6] medical diagnostics,[7–9] etc. However, it still remains great challenging to develop low-cost flexible visible-NIR photosensor and its arrays with excellent mechanical deformability and high optical detectivity for next-generation wearable electronics which could be conformally attached to human body with biocompatibility.[9] Conventional photodetectors based on inorganic crystalline materials such as Si, Ge, and InGaAs are normally fabricated on lattice-matched and rigid substrates, causing limited mechanical flexibility and tunability.[10,11] Their flexible counterparts would need a releasable strategy such as subsequent transfer process to allow its integration with flexible substrates. In contrast, organic materials have unmatchable advantages, such as tailorable absorption tunability, facile solution processability to render device

K. Pu, Z. Xu, Y. Gao, C. Zhao, G. Wei
Tsinghua-Berkeley Shenzhen Institute (TBSI)
Tsinghua Shenzhen International Graduate School
Tsinghua University
Shenzhen 518000, China
E-mail: guodan@umich.edu

K. Pu, Z. Xu, Y. Gao, C. Zhao, Y. Li, G. Wei
Institute of Materials Research
Tsinghua Shenzhen International Graduate School
Tsinghua University
Shenzhen 518000, China

The ORCID identification number(s) for the author(s) of this article can be found under https://doi.org/10.1002/admt.202300207

DOI: 10.1002/admt.202300207

F. Ershad, C. Yu
Department of Biomedical Engineering
Pennsylvania State University
University Park
Pennsylvania, PA 16802, USA
E-mail: cmy5358@psu.edu

R. Wang
Mountain View High School
Mountain View, CA 94040, USA

C. Yu
Department of Engineering Science and Mechanics
Department of Materials Science and Engineering
Materials Research Institute
Pennsylvania State University
University Park
Pennsylvania, PA 16802, USA

on a flexible substrate directly with superior flexibility and bendability.[12–15] In particular, visible-NIR organic photodetectors (OPD) with rationally designed materials and device architectures have been regarded as promising candidates for flexible imaging devices and wearable healthcare electronics whereas OPDs could have directly adhered onto curved surfaces through noninvasive and conformal integration strategies.[16,17] Organic thin films are usually solution processable and could be post-annealed at low temperature. Therefore, it is convenient to directly deposited on soft flexible substrates for large-area fabrication method such as inkjet printing and roll-to-roll which could potentially reduce their manufacture costs.[16] Specifically, the selection of narrow-bandgap organic semiconductors, including conjugated polymers,[18–20] metallo-organics,[21] and small molecules non-fullerene acceptors (NFA),[22] is critical for the fabrication of high-performance visible-NIR OPD.

The solution-processed bulk-heterojunction (BHJ) organic photodiodes have been increasingly investigated in visible-NIR detection. For example, Huang et al. reported a solution-processed BHJ OPD with thicker active layers based on a ultranarrow-bandgap NFA of CO1-4Cl, achieving a high maximum responsivity over 0.5 A W^{-1} and detectivity of 10^{12} Jones in the visible-NIR region beyond 900 nm.[23] Xie et al. exhibited a narrowband OPD with a full half-width maximum of ≈50 nm centered at 860 nm through intentional manipulation of the Frenkel exciton dissociation, obtaining a specific detectivity of more than 10^{13} Jones.[18] Though recent development of organic BHJ structure has greatly enhanced the photogeneration and charge collection efficiency, reaching detectivity up to 10^{13} Jones and solar cell conversion efficiency up to 19% under one sun illumination,[18,24] current challenges still remain to fabricate sensitive OPDs with high performance on a flexible substrate. On the one hand, it requires uniform and conformal thin film deposition of organic layers on a flexible substrate to reduce dark current; on the other hand, it simultaneously requires rational device design architecture with favorable energy level alignment to enhance efficient exciton dissociation and charge collection efficiency for enhanced quantum efficiency.

In this work, based on the narrow-bandgap non-fullerene acceptor materials named as BTP-4F, we report a solution-processed flexible OPD based on a blend of the donor D18 (dithieno[3', 2':3,4;2'',3'':5,6]benzo[1,2c][1,2,5]thiadiazole (DTBT) based polymer) as the photoelectric conversion material.[22,25,26] The molecular structure of the organic donor D18 contains a fused-ring acceptor unit, referred to as DTBT, which has a strong electron-withdrawing capability and extended larger molecular planes, enhancing π-π stacking and high hole mobility. The highly efficient narrow bandgap acceptor BTP-4F employs a ladder-type electron-deficient-core-based central fused ring with a benzothiadiazole core to fine-tune its absorption and electron affinity. Owing to low exciton binding energy of BTP-4F and preferred orientation of the active layer film on lamellar stacking, the D18:BTP-4F bulk heterojunction could facilitate exciton separation and charge transport. The obtained OPD has demonstrated superior photoelectrical properties, namely a large on/off current ratio under visible-NIR illumination.[27] Herein, due to the flexible nature of the stacked organic materials, the OPD based on a polyethylene naphthalate (PEN) substrate has shown excellent performance with a responsivity, specific detectivity, and response time of 206 mA W^{-1}, 6.45×10^{12} Jones (1 Jones = 1 cm $Hz^{1/2}$ W^{-1}), and 9 µs at the wavelength of 800 nm without applied bias, respectively, demonstrating 1000 continuous bending cycles at 150° test angle and 3 mm bending radius. To note, a unique flexible visible-NIR image sensor was successfully achieved with a 5 × 5 array for the detection of uniform multipoint light distribution and fast identification of target images even when the device was bent. Therefore, the collective results on blend film design, flexible device fabrication and characterization, and imager development shed light on sought-after visible-NIR photosensing and imaging systems.

2. Result and Discussion

As shown in **Figure1**a, the flexible OPD with a configuration of ITO/PEDOT:PSS/D18:BTP-4F /Phen-NaDPO/Ag was fabricated on a PEN substrate. The corresponding energy level alignment and molecular structure of organic materials are illustrated in Figure 1b-d. PEDOT:PSS has been employed as an effective hole transport layer, in the meantime, it also works as a buffer layer for subsequent device fabrication. The wetting processes play an important role in the active layer of D18:BTP-4F to be deposited on the flexible PEN substrate, which is not as smooth as glass substrate. Phen-NaDPO acted as an electron transport layer to facilitate effective electron charge collection. As depicted in Figure 1e, the D18 film exhibits a visible absorption region from ≈410 to 620 nm. BTP-4F film exhibits a broad absorption in the range from 520 to 950 nm with a relatively intense peak at 840 nm. Not surprisingly, the absorption spectra of the D18:BTP-4F film is similar to the superposition of the respective spectra obtained from these two compounds. Due to its broad absorption region from visible to NIR, the D18:BTP-4F bulk film served as the active layer in the as-obtained OPDs. The charge carrier dynamics at the D18/BTP-4F interface was investigated by measuring the photoluminescence (PL) spectra of neat D18, neat BTP-4F, and blend films as exhibited in Figure 1f. It is apparent that D18 exhibited a peak at 670 nm, and the BTP-4F film exhibited a peak at 880 nm. When blending D18 and BTP-4F, the PL emission peaks of D18 and BTP-4F were quenched, which indicates effective exciton separation and charge transfer occur. The morphological characteristics were further explored by scanning electron microscopy (SEM) and atomic force microscopy (AFM), as shown in Figure 1g,h. Randomly distributed nanowires can be seen due to the high crystallinity of D18, indicating an interconnecting network for hole transport. Meanwhile, the roughness, which was as low as 2.64 nm, indicated a smooth and high-quality thin film for charge transport. Therefore, the observed morphological characteristics of the film ensure that a high-quality, uniformly patterned 5 × 5 matrix on PEN substrates can be fabricated for imaging applications (Figure S1, Supporting Information).

In order to investigate the influences of the active layer thicknesses on the photodetection performance, three OPDs with different active layer thicknesses from 55 nm, 100 nm, and 145 nm were carried out. The external quantum efficiency (*EQE*) spectra of the OPDs without applied bias are shown in **Figure2**a. It is known that the *EQE* values of OPDs are determined by the photon absorption, exciton dissociation, and charge collection.

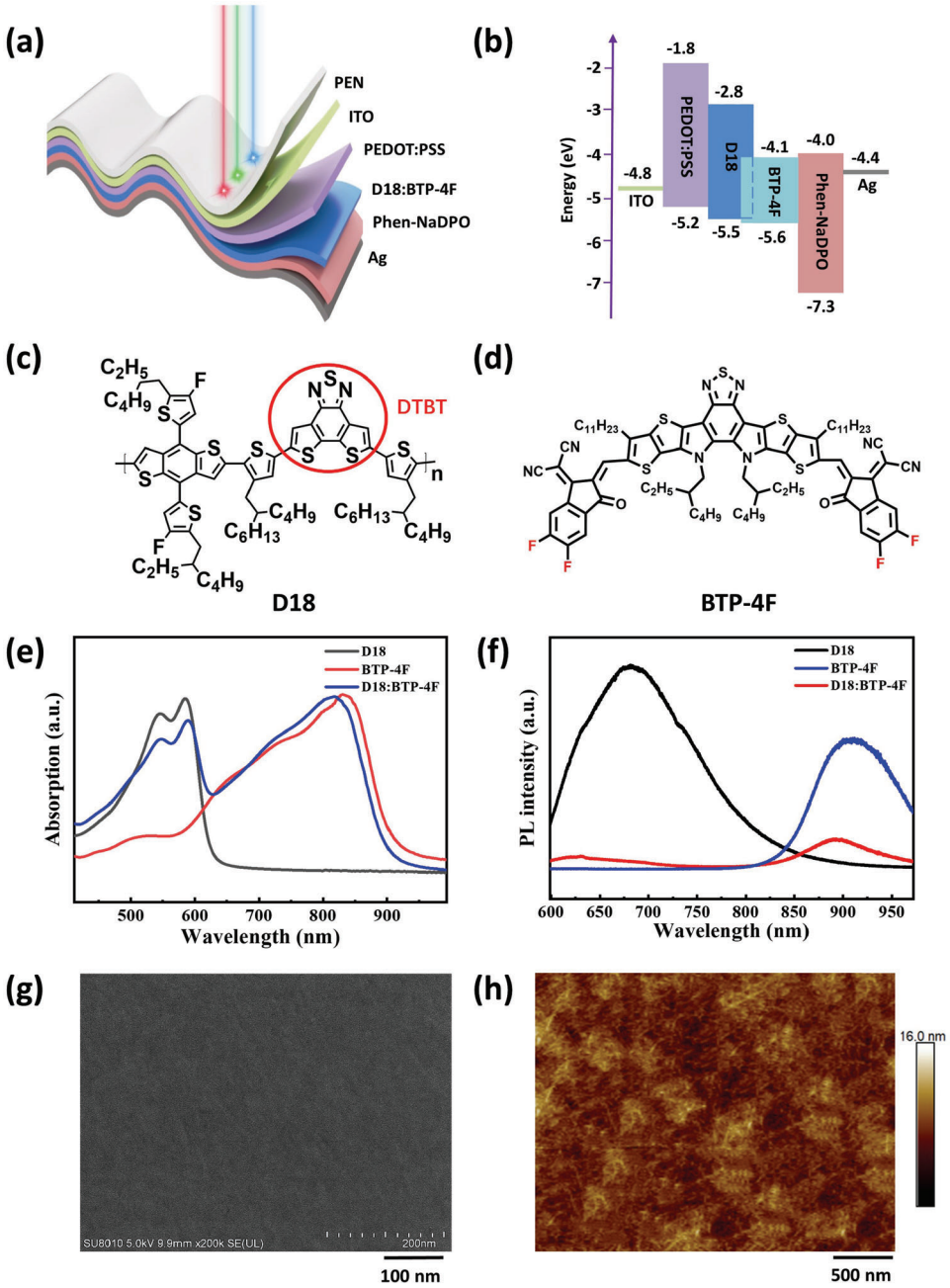

Figure 1. a) Schematic diagram of the device structure. b) The energy level matching diagram of the device. c,d) The molecular structures of D18 and BTP-4F, respectively. e) The absorption spectra of neat D18, neat BTP-4F, and D18:BTP-4F blend films. f) The photoluminescence spectra of neat D18, neat BTP-4F, and D18:BTP-4F blend films. g,h) The SEM and AFM images of D18:BTP-4F film, respectively.

Though a thicker active layer is necessary to improve light absorption, it is beneficial to deposit thinner layer to increase charge collection efficiency. The *EQE* could reach the maximum value of 63% at the wavelength of 500 nm with the active layer thickness of 100 nm. In addition, there is a relatively small difference from the *EQE* on regular glass substrates plotted in Figure S2, Supporting Information. To note that the *EQE* does not exactly correspond to the absorption spectrum due to the effect of the absorption of the PEN substrate, shown in Figure S3, Supporting Information. The responsivity (R) was determined according to the following equation:

$$R = \mathrm{EQE} \times \frac{e\lambda}{hc} \tag{1}$$

where e, λ, h, and c represent the absolute value of electronic charge, the light wavelength, the Planck constant, and the speed of light, respectively. As can be seen from Figure 2b, the R of the OPD with 100 nm active layer thickness are 0.270 A W^{-1} and 0.206 A W^{-1} at 540 nm and 800 nm, respectively. An important

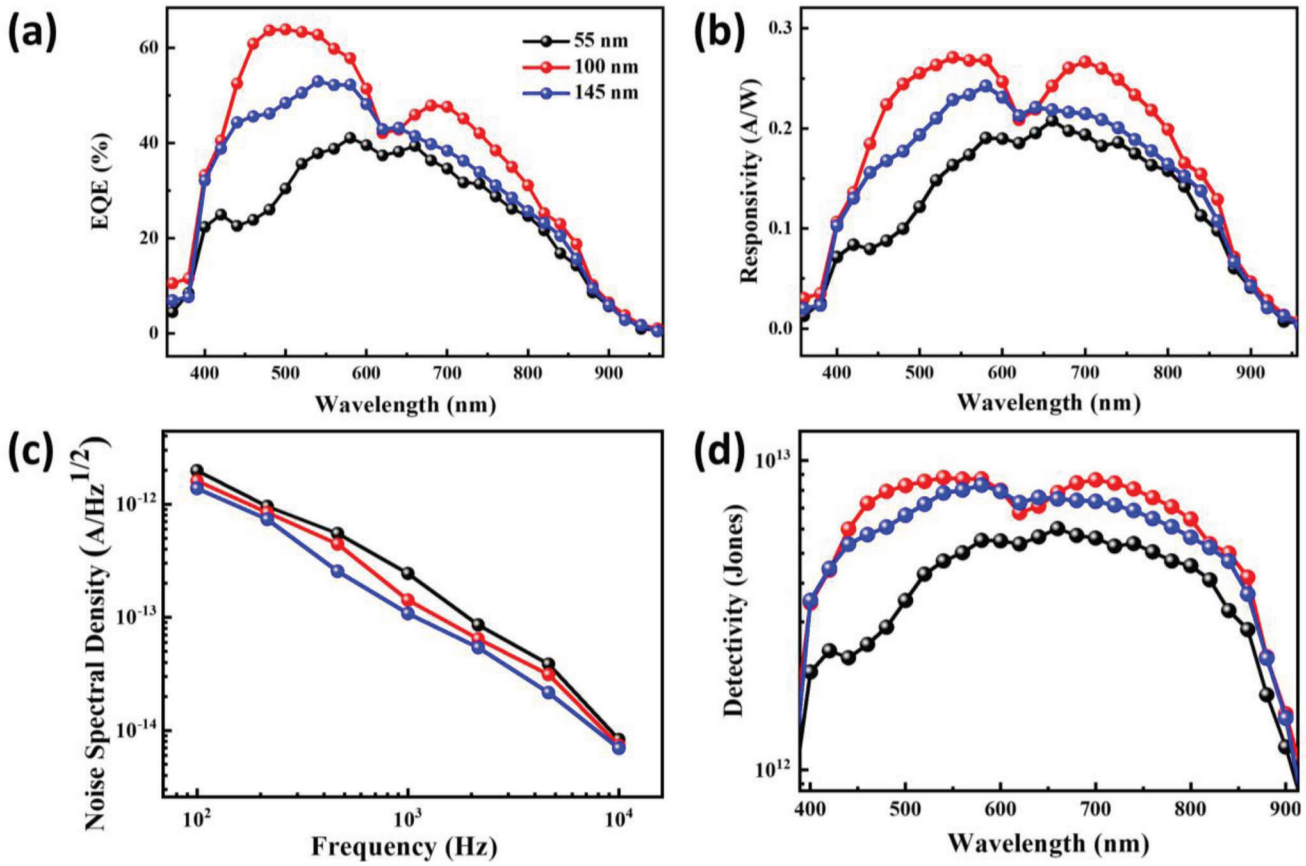

Figure 2. Performance description of OPD with different active layer thickness. a) The EQE of the OPD dependence wavelength. b) The responsivity dependence on wavelength. c) Noise spectral density of the OPD. d) The detectivity dependence on wavelength.

figure-of-merit of OPD is the specific detectivity (D^*), which describes the sensitivity to low light. the value of D^* could be accurately detected by measuring the noise current, which can be calculated as follows:

$$D^* = \frac{\sqrt{A}}{NEP} = \frac{R\sqrt{A}}{\sqrt{i_{noise}}} \quad (2)$$

where NEP, A, and i_{noise} are the noise equivalent power, the effective irradiation area, and the noise current, respectively. The noise spectral density of devices was shown in Figure 2c. The noise current was found to decrease slightly with increasing active layer thickness, mainly due to the reduction of extrinsic defects (e.g., film imperfections, pinholes, and other leakage paths).[28] According to the above formula (2), taking the noise spectral density at 1×10^4 Hz, the D^* value of the OPD with active layer of 100 nm reached a maximum after optimizing the responsivity and noise current, and was calculated to be 6.45×10^{12} Jones at 800 nm without applied bias as shown in Figure 2d. The device shows high optoelectronic performance compared to the reported OPD based on the BTP-4F non-fullerene acceptor.[18,29,30]

The effect of the applied bias voltage on the optical photoresponse of OPD as shown in **Figure3**a. The reverse bias voltage applied to the D18:BTP-4F bulk junction has extended the depletion region and enhanced the built-in electric field, indicating good typical diode behavior. As displayed in Figure 3b, with increasing continuous light intensity from 3.40×10^{-7} to 6.82×10^{-2} W cm^{-2} of 800 nm at the bias voltages of 0 V, the photocurrent increased linearly, resulting in an exceptionally high on/off ratio of ≈10^5. A fitting analysis yielded that the photocurrent is linearly proportional to the incident light intensity, indicating efficient charge separation and transport.[31] The linear dynamic region (LDR) describes the response range with varied incident light intensities.[11] It can be calculated with

$$\mathrm{LDR} = 20\lg\left(\frac{J_{\max}}{J_{\min}}\right) \quad (3)$$

where $J_{\max}$ and $J_{\min}$ are the maximum and minimum of the linear portion of the photocurrent, respectively. In the region of linear photosensitivity for the OPD, $J_{\max}$, and $J_{\min}$ were measured to be 1.36×10^{-2} and 1.29×10^{-7} A cm^{-2}, respectively. The LDR of the OPD is 100 dB, which is comparable with that of organic photodetectors in the literature.[33] Response time is a direct reflection of OPD performance. The rise time (τ_{rise}) and decay time (τ_{decay}) are defined as the time interval for the current to increase from 10% to 90% and to decrease from 90% to 10%, respectively.[11] Figure 3c presents a single cycle, where $\tau_{\mathrm{rise}}/\tau_{\mathrm{decay}}$ of 9.3/8.7 μs can be accurately determined, suggesting an ultrafast response. Figure 3d shows that the 3 dB frequency, where the response is

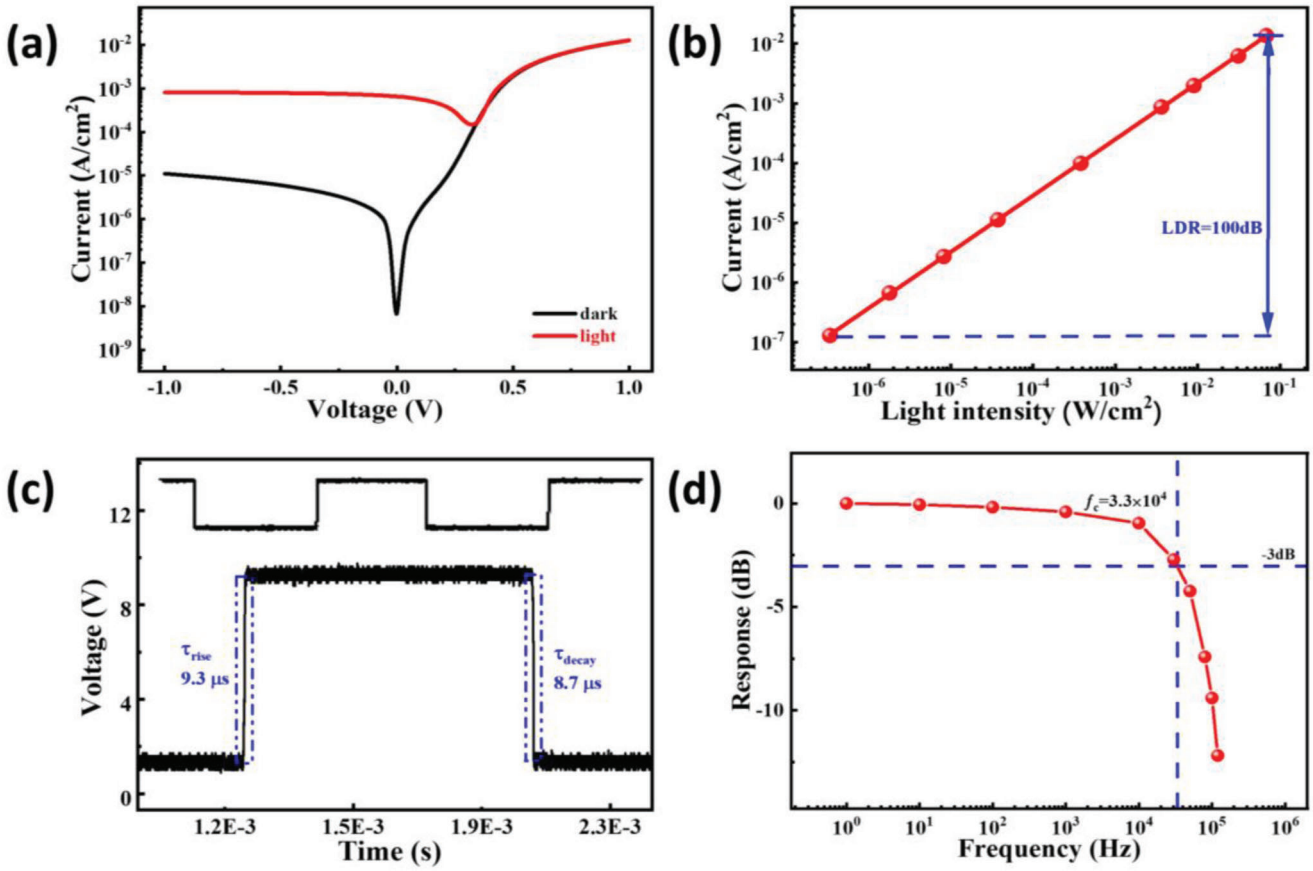

Figure 3. a) The *J–V* curves of the OPD. b) The photocurrent dependence on light intensity. c) Response time including rise and decay time, inset is the current-time curve. d) Normalized response under a series of light frequencies.

reduced from 1 to 0.707, is 3.3×10^4 Hz. The value of the frequency domain response also corresponds to the time-dependent response at the microsecond level. This characteristic indicates that the OPD could detect various rapid illumination frequencies and demonstrate excellent reproducibility. Further, an active layer of PM6:BTP-4F was used to replace D18:BTP-4F to illustrate the universal applicability of the manufacturing method and the generality of the conclusion. As shown in Figure S4, Supporting Information, the OPD with PM6:BTP-4F exhibits excellent performances with the *R*, D^* and response time of 174 mA W^{-1}, 4.18×10^{12} Jones, and 14.6 μs at the wavelength of 800 nm and bias voltage of 0 V, which is comparable to the performance of that based on the photoactive layer of D18:BTP-4F.

Folding resistance and flexibility are the key parameters of flexible devices.[9] The electrical stability of the OPDs under various bending conditions was characterized. **Figure4**a shows images of the device under different bending angles, where the bending angle is defined as the corner between the tangent line of one side and the other side of the flexible device. Figure 4b shows the output current of the OPDs under different test angles at a bending radius of 3 mm, under dark and 800 nm NIR illumination with 0.08 μW, respectively. Both the dark current and photocurrent do not change significantly under different bending angles, indicating that the devices still maintain excellent electrical stability after large-angle bending. As can be seen from Figure 4c, the millimeter-level curvature has little effect on device performance, making the flexible OPDs suitable for wearable devices and curved imaging.[8] Maintaining device performance after several cycles of bending is also vital for practical applications of flexible electronic devices. Figure 4d shows the *I–V* curves of the flexible device before and after different numbers of bending cycles at a radius of curvature of 3 mm and a test angle of 150°. The corresponding dark characteristic curves were shown in Figure S5, Supporting Information. It can be clearly seen that even after 200 bending cycles, the performances are almost identical to those of the unbent devices. After bending 1000 times, the photocurrent still stays at the same level, indicating the superior folding resistance as-fabricated photodetector exhibited.[18] Figure 4e shows a light response time of 10 μs, even after 200 cycles of 150° large-angle bending. The OPD shows the same ultrafast response compared to that of the initial device, indicating that the bending did not decrease the response time. These results demonstrate the high flexibility of D18:BTP-4F flexible devices that could be implemented as flexible wearable devices for visible-NIR sensing and imaging. Meanwhile, the OPD with active layer of PM6:BTP-4F was also tested for flexibility as shown in Figure S6, Supporting Information, and showed the same superior performance compared with D18:BTP-4F film. To explain the high bendability of the OPDs, the morphology of pure BTP-4F and D18:BTP-4F films on flexible substrates was compared after

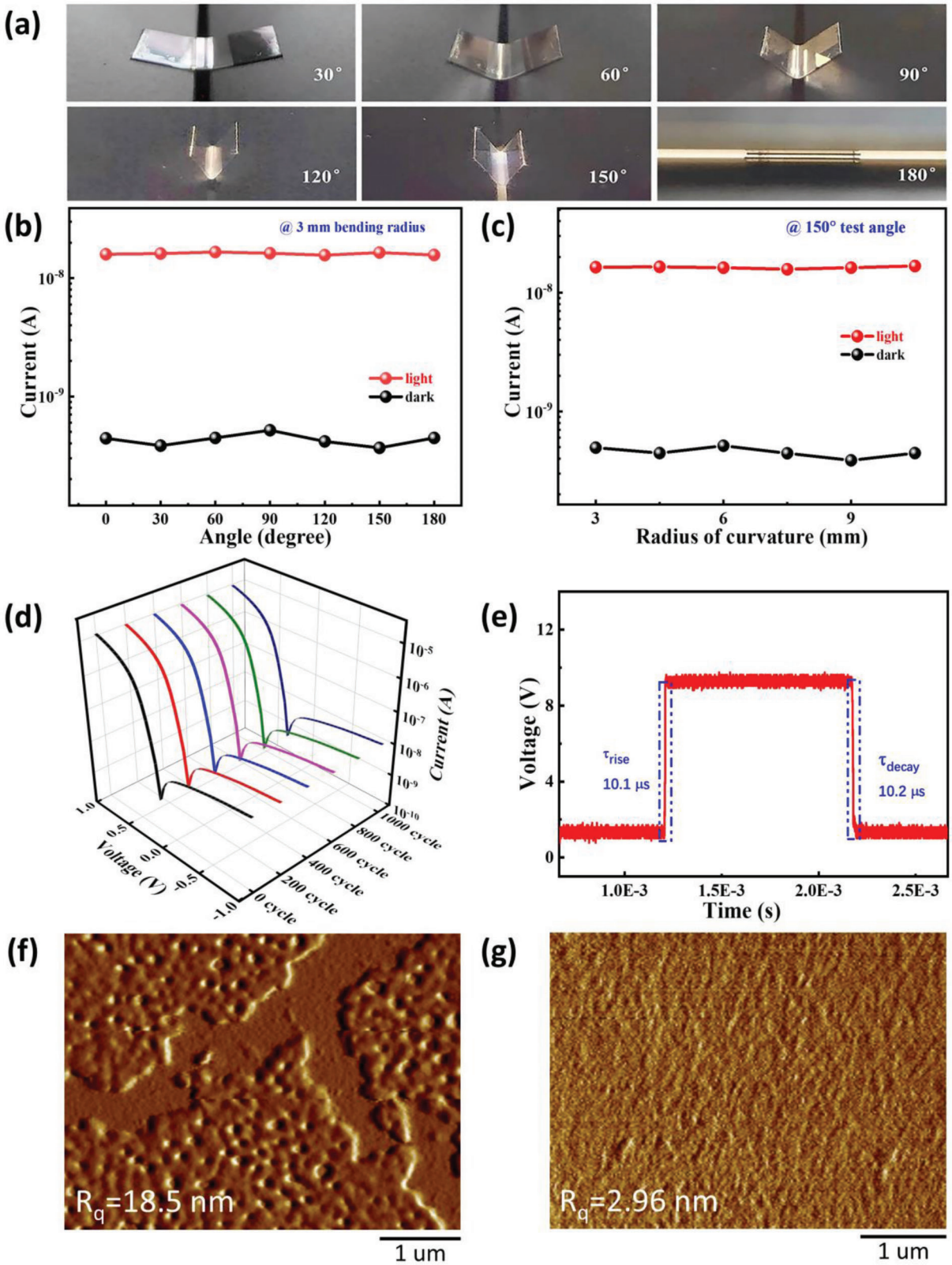

Figure 4. a) The optical images of devices under different bending conditions. b,c) The current of the OPD under different bending angles. and radii of curvature, respectively. d) *I–V* curves of the device under 800 nm light illumination after 0, 200, 400, 600, 800, and 1000 cycles of bending with test angle of 150° and bending radius of 3 mm. e) Response cycle to estimate the rise and decay time after 200 cycles of bending. f) The AFM image of neat BTP-4F film after 200 cycles of bending. g) The AFM image of D18:BTP-4F film after 200 cycles of bending.

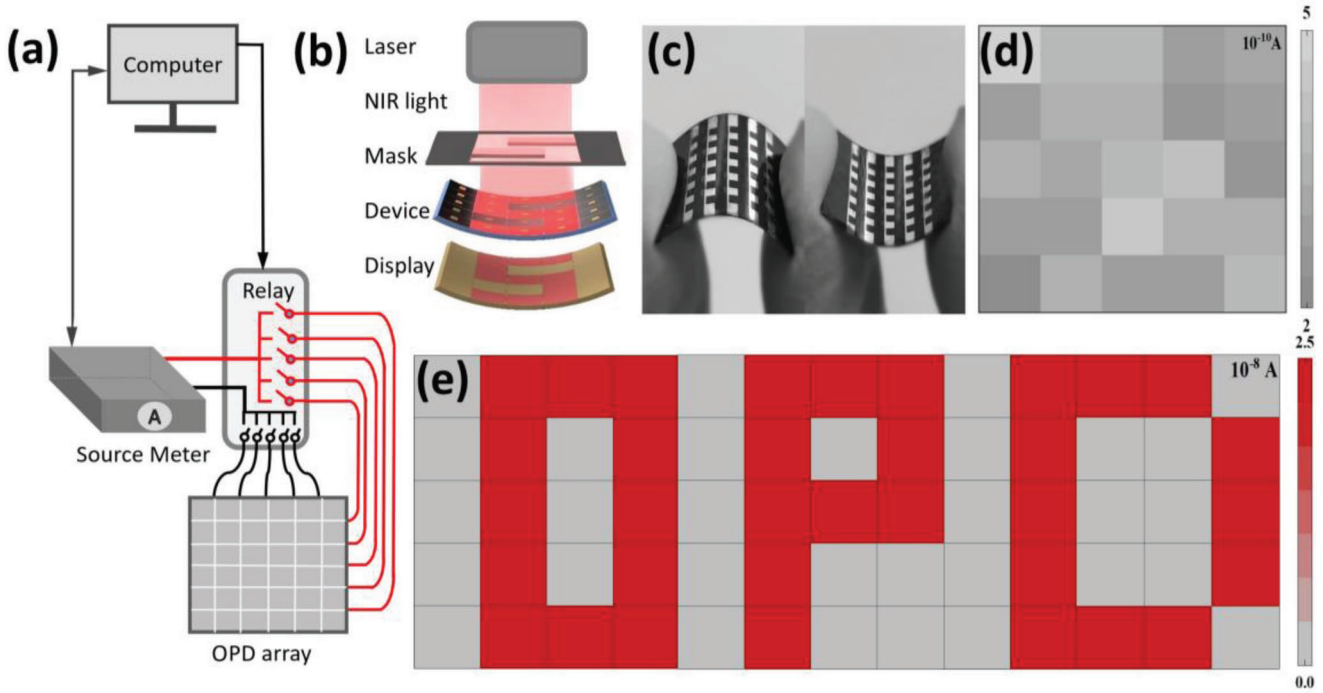

Figure 5. a) Schematic illustration of the signal acquisition system. b) Schematic illustration of the image sensing setup. c)The sample images of the flexible image sensor with different bending directions. d) The uniformity test of dark current. e) The corresponding sensing results, where the image sensor was separately illuminated with 850 nm light in the patterns of the letters "O", "P", and "D".

200 cycles of bending. As shown in Figure 4f,g, the pure BTP-4F film had numerous cracks and possessed a large roughness of 18.7nm, while the D18:BTP-4F film remained integrity and had a smoother surface. It is probable that the interconnected network formed by the D18 polymer can release stress and reduce the strain.

Wearable devices based on flexible OPD can be employed for health monitoring. the blood flowing in the subcutaneous tissue can conclude most basic human features,[18] which can be detected with near-infrared light allowing for low-cost, non-invasive optical monitoring. As illustrated with the setup in Figure S7, Supporting Information, the OPD detects changes in blood volume during each cardiac cycle when near-infrared light from the OLED illuminates human tissue. These changes can be converted into electrical signals as shown in Figure S8, Supporting Information, which are collected to assess the heart rate. Heart rate signals from one of the authors showed 11 cycles in 9 seconds, meaning 73 beats per minute.

Furthermore, a 5×5 OPD array with 25 pixels was developed to illustrate a practical example of such visible-NIR OPD for imaging applications. There are two main common readout methods available for the light intensity received by each cell within an image sensor. One is by combining a switching element and a photodetector in each cell. However, it can be easily affected by wiring noise and crosstalk, both of which are caused by the low amount of signal received from each cell. The other method is to integrate an amplifier circuit, a photodetector, and a switching element in each cell. The main noises are reset noise associated with reset operation and the fixed pattern noise due to performance variations in amplifiers in each pixel.[7] In this study, we use a computer-controlled relay to select the line to be switched on and a Source Meter to collect the signal, which substantially reduces noise and crosstalk compared to the above two methods and ensures the accuracy of the data obtained. The schematic diagram of the current acquisition system is shown in **Figure 5**a. The signal of each pixel is transmitted by two mutually perpendicular cross electrodes. Figure 5b shows the image sensing setup and path of optical transmission. Three masks with different letters "O", "P", and "D" were separately placed between the laser and the OPD array. When the 850 nm LED is turned on during image sensing measurements, light is passed through the mask, projecting each letter directly on the flexible image sensor with 25 pixels. It is critical to verify the uniformity of the light response performance of all pixels. The sample images of the device with different bending directions are shown in Figure 5c. Figure 5d shows the dark current distribution of the flexible image sensor, which exhibits adequate uniformity of the device. The three images in Figure 5e show the imaging results, which were separately obtained by illuminated the mask with the different letters. The shape of the three letters contrasts with the background and is easily distinguishable, showing the great promise of OPD arrays in next-generation optoelectronics.

3. Conclusion

In conclusion, we have successfully developed a D18:BTP-4F blend-based flexible visible-NIR self-powered photodetectors with a facile solution process. The active layer thicknesses of D18:BTP-4F layer have been optimized as 100 nm to maximize

the photocurrent as well as suppressing dark current. Owing to the well-formed D18:BTP-4F bulk heterojunction, the device was vertically sandwiched for effective charge generation, featuring high responsivity (up to 206 mA W^{-1}), specific detectivity (up to 6.45×10^{12} *Jones*), and fast response time (≈9 µs). In addition, the OPD based on a PEN substrate showed up to 1000 bending/releasing cycles with an angle of 150° at a radius of curvature of 3 mm, indicating excellent flexibility, mechanical robustness, and cyclic folding endurance. The obtained OPD has reliable linear photosensitivity as demonstrated by the response of different incident light intensities. Furthermore, the flexible visible-NIR image sensor for imaging acquisition is shown by demonstrating 5×5 OPD array. The flexible and low-cost visible-NIR OPDs hold great promise in photosensing and imaging for a variety of emerging future applications, ranging from optical communication, continuous health monitoring sensors, and flexible image sensors to wearable devices.

4. Experimental Section

Materials: PEN/ITO was purchased from South China Xiangcheng Technology; PEDOT:PSS was purchased from Heraeus; Chloroform was purchased from Sigma Aldrich; D18 and BTP-4F were purchased from Shanghai Weizhu Chemical Technology Co. Ltd; Phen-NaDPO was purchased from Puri Material Technology Co. Ltd. Ethanol was purchased from Alfa Aesar.

Fabrication of Photovoltaic Devices: ITO-coated PEN substrates were cleaned with plasma, and then device with ITO/PEDOT:PSS/D18:BTP-4F/Phen-NaDPO/Ag structures is fabricated. First, the ≈40 nm PEDOT:PSS layer is spin-coated onto the ITO-coated PEN substrate, and then thermally annealed on a hot plate at 110°C. The substrate is transferred into a N_2-golvebox and the D18:BTP-4F active layer was spin-coated from D18:BTP-4F (1:1.6 by weight) chloroform solution onto the PEDOT:PSS layer, followed by solvent annealing of CF in a covered Petri dish. Afterward, Phen-NaDPO layer was spin-coated on top of D18:BTP-4F layer from Phen-NaDPO solution (0.5 mg ml^{-1} ethanol). Finally, Ag is thermally evaporated under a shadow mask.[34] The fabrication process for imaging arrays and photodetectors is similar.

Characterization of Photovoltaic Devices: The equipment used in this experiment mainly includes Scanning electron microscopy (SU8010, HITACHI), surface profilometer (MDTC-EQ-M16-01, Bruker Dimension Icon), HP 8453 spectrophotometer (used to measure UV–vis absorption spectra and transmittance spectra), and *I–V* testing system (YSL SC-pro7, Zolix). The noise current was measured by an electrically shielded and optically sealed probe station and connected in series with a Stanford Research SR830 lock-in amplifier.[35]

Collection of Sensor Array Signals: Signal measurements were carried out with the *I–V* testing system (YSL SC-pro7, Zolix). Three masks with different letters were separately placed between the laser and the OPD array. When the 850 nm LED is turned on during image sensing measurements, light is passed through the mask, projecting each letter directly on the flexible image sensor. Two cross electrodes perpendicular to each other transmit signals for each pixel. A computer-controlled relay is used to select the line to be switched on.

Health Monitoring: All participants have provided written consent for the participants of the heart rate measurement, which is detected with near-infrared light directly illuminated at one index finger.

Supporting Information

Supporting Information is available from the Wiley Online Library or from the author.

Acknowledgements

The authors thank funding support from the National Natural Science Foundation of China (Grant Number: 52027817), the Science and Technology Planning Project of Shenzhen Municipality (Grant number: GJHZ20210705143204013).

Conflict of Interest

The authors declare no conflict of interest.

Author Contributions

G.D.W., K.P., F.Y.K., and C.Y. conceived the ideas and coordinated the work. K.P., Z.H.X., and Y.G. carried out the device fabrication and test. C.Z. helped device test setup. G.D.W. guided the experiment. F.E., R.W. discussed and revised this manuscript. All authors revised and commented on the manuscript.

Data Availability Statement

Research data are not shared.

Keywords

flexibility, organic photodetectors, solution-processes, visible-NIR imaging

Received: February 13, 2023
Revised: March 6, 2023
Published online: April 6, 2023

[1] X. Huang, Q. Li, W. Shi, K. Liu, Y. Zhang, Y. Liu, X. Wei, Z. Zhao, Y. Guo, Y. Liu, *Small* **2021**, *17*, e2102820.
[2] C. Rogers, A. Y. Piggott, D. J. Thomson, R. F. Wiser, I. E. Opris, S. A. Fortune, A. J. Compston, A. Gondarenko, F. Meng, X. Chen, G. T. Reed, R. Nicolaescu, *Nature* **2021**, *590*, 256.
[3] D. Li, J. Du, Y. Tang, K. Liang, Y. Wang, H. Ren, R. Wang, L. Meng, B. Zhu, Y. Li, *Adv. Funct. Mater.* **2021**, *31*, 2105887.
[4] S.-H. Lee, A. R. b. M. Yusoff, C. Lee, S. C. Yoon, Y.-Y. Noh, *Mater. Sci. Eng.: R: Rep.* **2022**, 147, 100660.
[5] K. D. Hakkel, M. Petruzzella, F. Ou, A.van Klinken, F. Pagliano, T. Liu, R. P. J.van Veldhoven, A. Fiore, *Nat. Commun.* **2022**, *13*, 103.
[6] G. Konstantatos, *Nat. Commun.* **2018**, *9*, 5266.
[7] T. Yokota, K. Fukuda, T. Someya, *Adv. Mater.* **2021**, *33*, 2004416.
[8] S. Cai, X. Xu, W. Yang, J. Chen, X. Fang, *Adv. Mater.* **2019**, *31*, 1808138.
[9] P. C. Y. Chow, T. Someya, *Adv. Mater.* **2020**, *32*, 1902045.
[10] F. P. García de Arquer, A. Armin, P. Meredith, E. H. Sargent, *Nat. Rev. Mater.* **2017**, *2*, 16100.
[11] J. Liu, M. Gao, J. Kim, Z. Zhou, D. S. Chung, H. Yin, L. Ye, *Mater. Today* **2021**, *08*, 004.
[12] L. Li, H. Chen, Z. Fang, X. Meng, C. Zuo, M. Lv, Y. Tian, Y. Fang, Z. Xiao, C. Shan, Z. Xiao, Z. Jin, G. Shen, L. Shen, L. Ding, *Adv. Mater.* **2020**, *32*, 1907257.
[13] X. W. Tong, Y. N. Lin, R. Huang, Z. X. Zhang, C. Fu, D. Wu, L. B. Luo, Z. J. Li, F. X. Liang, W. Zhang, *ACS Appl. Mater. Interfaces* **2020**, *12*, 53921.
[14] Y. L. Wu, K. Fukuda, T. Yokota, T. Someya, *Adv. Mater.* **2019**, *31*, 1903687.
[15] X. Gong, M. Tong, Y. Xia, W. Cai, J. S. Moon, Y. Cao, G. Yu, C.-L. Shieh, B. Nilsson, A. J. Heeger, *Science* **2009**, *325*, 1665.

[16] Y. Wei, H. Chen, T. Liu, S. Wang, Y. Jiang, Y. Song, J. Zhang, X. Zhang, G. Lu, F. Huang, Z. Wei, H. Huang, *Adv. Funct. Mater.* **2021**, *31*, 2106326.
[17] D. Yang, D. Ma, *Adv. Opt. Mater.* **2019**, *7*, 1800522.
[18] H. Ren, J. D. Chen, Y. Q. Li, J. X. Tang, *Adv. Sci.* **2020**, *8*, 2002418.
[19] B. Xie, R. Xie, K. Zhang, Q. Yin, Z. Hu, G. Yu, F. Huang, Y. Cao, *Nat. Commun.* **2020**, *11*, 2871.
[20] A. E. London, L. Huang, B. A. Zhang, M. B. Oviedo, J. Tropp, W. Yao, Z. Wu, B. M. Wong, T. N. Ng, J. D. Azoulay, *Polym. Chem.* **2017**, *8*, 2922.
[21] D. Meng, R. Zheng, Y. Zhao, E. Zhang, L. Dou, Y. Yang, *Adv. Mater.* **2021**, *34*, 2107330.
[22] M. S. Choi, S. Chae, H. J. Kim, J. J. Kim, *ACS Appl. Mater. Interfaces* **2018**, *10*, 25614.
[23] Y. Yang, *ACS Nano* **2021**, *15*, 18679.
[24] J. Huang, J. Lee, J. Vollbrecht, V. V. Brus, A. L. Dixon, D. X. Cao, Z. Zhu, Z. Du, H. Wang, K. Cho, G. C. Bazan, T. Q. Nguyen, *Adv. Mater.* **2020**, *32*, 1906027.
[25] W. Gao, F. Qi, Z. Peng, F. R. Lin, K. Jiang, C. Zhong, W. Kaminsky, Z. Guan, C. S. Lee, T. J. Marks, H. Ade, A. K. Jen, *Adv. Mater.* **2022**, *34*, 2202089.
[26] Q. Liu, Y. Jiang, K. Jin, J. Qin, J. Xu, W. Li, J. Xiong, J. Liu, Z. Xiao, K. Sun, S. Yang, X. Zhang, L. Ding, *Sci. Bull.* **2020**, *65*, 272.
[27] J. Yuan, Y. Zhang, L. Zhou, G. Zhang, H.-L. Yip, T.-K. Lau, X. Lu, C. Zhu, H. Peng, P. A. Johnson, M. Leclerc, Y. Cao, J. Ulanski, Y. Li, Y. Zou, *Joule* **2019**, *3*, 1140.
[28] L. Zhu, J. Zhang, Y. Guo, C. Yang, Y. Yi, Z. Wei, *Angew. Chem., Int. Ed.* **2021**, *60*, 15348.
[29] G. Simone, M. J. Dyson, S. C. J. Meskers, R. A. J. Janssen, G. H. Gelinck, *Adv Funct Mater* **2019**, *30*, 1904205.
[30] Z. Zhao, J. Wang, C. Xu, K. Yang, F. Zhao, K. Wang, X. Zhang, F. Zhang, *J. Phys. Chem. Lett.* **2020**, *11*, 366.
[31] K. Yang, J. Wang, Z. Zhao, F. Zhao, K. Wang, X. Zhang, F. Zhang, *Org. Electron.* **2020**, *83*, 105739.
[32] B. Nie, J. G. Hu, L. B. Luo, C. Xie, L. H. Zeng, P. Lv, F. Z. Li, J. S. Jie, M. Feng, C. Y. Wu, Y. Q. Yu, S. H. Yu, *Small* **2013**, *9*, 2872.
[33] Y. Song, G. Yu, B. Xie, K. Zhang, F. Huang, *Appl. Phys. Lett.* **2020**, *117*, 093302.
[34] W. Xu, Y. Gao, K. Qian, B. Wang, R. Xu, M. He, T. Li, G. Xing, S. Yang, G. Wei, *J. Mater. Chem. C* **2022**, *10*, 9391.
[35] Y. Gao, C. Zhao, K. Pu, M. He, W. Cai, M. C. Tang, F. Kang, H. L. Yip, G. Wei, *Kexue Tongbao (Foreign Lang. Ed.)* **2022**, *67*, 1982.